Supplementary Information

Dissecting Ionic Favorable Hydrogen Bond Chemistry in Hybrid Separator for Aqueous Zinc-Ion Batteries

Yixiu Wang, ‡ [a] Heng Zhou, ‡ [a] Shiqiang Wei,*[a] Hengjie Liu,[a] Shuangming Chen,*[a] Xin Chen,[c] Kefu Zhu,[a] Xunshuang Zhang,[a] Yang Si,[a] Xiaojun Wu,[b] Ran Long,[a] Liangbin Li,[a] and Li Song*[a]

1. Experimental methods

Materials Preparation. Boron nitride (BN) modified polyacrylonitrile (PAN) separators were prepared by non-solvent thermal phase separation method using a blade coating method. 36.25 mL of dimethyl sulfoxide (DMSO) was mixed with 5 mL of DI water by stirring for 30 min. Then, 1 g of BN powder was added and stirred for an additional 30 min, followed by the addition of 5 g polyacrylonitrile (M_W=1000000), which was stirred for another 30 min. For the preparation of the pure polyacrylonitrile separator, BN powder was not added. The stirred solution was heated at 60 ℃ for 3 h and then at 80 ℃ for 3 h. During this period, the solution was stirred every 40 min for 30 min. The obtained solution was poured onto a stainless-steel substrate that had been preheated to 70°C, and the film was scraped with a 750 μm preparator. After resting for 10 min, the film was transferred to DI water to remove the solvent and washed again with water changes every 12 h for a total of 4 times. Additionally, the size of the BN-PAN separator was determined by the size of the coated substrate and the preparator. The maximum width of the lab-scale separators was 7.5 cm and the maximum length was 20 cm, using a stainless-steel substrate with a length of 28 cm and a preparator with a width of 10 cm. The separators with greater surface areas could be fabricated by employing larger scrapers and substrates. NVO cathode was prepared by a hydrothermal method. 0.64 g NH_4VO_3 was

added to 80 mL of deionized water and stirred at 60 ℃ in an oil bath. 1.16 g $H_2C_2O_4 \cdot 2H_2O$ was added to the above solution and stirred until dissolved. The solution was transferred to a 100 mL autoclave and reacted at 180 ℃ for 4 h. The product was washed with DI water and ethanol 5 times, centrifuged at 8000 rpm, and dried in a vacuum oven at 60 ℃ for 12 h.

Characterizations. The X-ray diffraction (XRD) data was obtained by using a Multifunctional Rotating-anode X-ray Diffractometer (SmartLab) with Cu radiation (λ=1.54 Å). Scanning electron microscope (SEM: SU8220) was used to observe the of morphology samples. The Fourier transform infrared spectroscopy (FTIR) was taken by using the Fourier transform infrared spectrometer (Nicolet 8700). Synchrotron radiation small-angle X-ray scattering (SR-SAXS) and wide-angle X-ray scattering (SR-WAXS) tests were carried out at the beamline BL10U1 in Shanghai Synchrotron Radiation Facility. The nitrogen absorption/desorption isotherms were obtained by surface area and porosity analyzer (Micromeritics ASAP 2460). The contact angle of 2 M $ZnSO_4$ electrolyte on the surface of the separators was obtained by using optical contact angle measuring instrument (Theta Flex). Thermogravimetric analysis (TGA: SDT 650) was utilized to test the thermal stability of the separators. The X-ray photoelectron spectrometer (XPS) analysis was conducted obtained with an Al Kα spectrometer (Thermo Scientific ESCALAB 250Xi). *In situ* FTIR was carried out at Infrared spectroscopy and microspectroscopy (BL01B) in Hefei Synchrotron Radiation Facility. XAFS measurement for Zn K-edge was launched at the beamline BL14W1 in Shanghai Synchrotron Radiation Facility.

Electrochemical measurements. Electrochemical measurements were taken with CR-2032 coin-type cell. Zn//Zn and Zn//Cu batteries were assembled by using zinc metal foils with thickness of 100 μm and 12 mm in diameter as anode, 100 μL 2 M $ZnSO_4$ as electrolyte and BN-PAN or PAN membranes as separator. Cu foil with the radius of 8 mm as cathode in Zn//Cu batteries, respectively. The cathode materials for full batteries consisted of NVO (~30 mg), Super P and polyvinylidene fluoride (PVDF) with a mass ratio of 7:2:1. The three components were mixed in a mortar and grinded for 15 minutes. 200 μL N-methyl-2-pyrrolidone (NMP) was added into the mixture and further grinded for 15 minutes. The stainless steel meshes of 1000-mesh were used as electrode current collectors, which were cut into circles with the radius of 6 mm, washed with ethanol solution in ultrasonic machine and dried in the 70 ℃ oven. The prepared cathode slurry was coated onto the stainless steel meshes, pre-dried in the 70 ℃ oven for 30 minutes and then transferred to the 100 ℃ vacuum oven for 12 hours. The average mass loading of the active material is about 1.025 mg cm^{-2}. The cathode material of Zn-I_2 full battery was made up of I_2/active carbon, Super P and PVDF with a mass ratio of 8:1:1. The I_2/active carbon material was first mixed with a ratio of 1:2 and then heated at 100 ℃ for 12 h before use. The carbon cloth with the radius of 6 mm was used as electrode current collectors. The coating process of the cathode material was the same as that described above for the NVO cathode. After coating, the prepared cathode was dried in the 25℃ oven for 24 hours. The average mass loading of the active material for Zn-I_2 full battery is about 2.853 mg cm^{-2}. CV, EIS, Tafel plots, LSV and amperometric i-t curve were performed on the electrochemical work-station (CHI660D, Shanghai CH Instrument Company, China). The EIS spectrograms were obtained from the above-mentioned

electrochemical workstation starting from open circuit potential over the frequency range from 10^5 to 0.01 Hz. The rate performance, cycling stability and galvanostatic intermittent titration technique (GITT) of the cell were measured on the Land CT2001A battery test system at the 25 ℃ thermostat. The voltage ranges for Zn//NVO cell and Zn-I_2 cell were 0.2-1.6 V and 0.6-1.7 V, respectively. The flexible pouch cells were assembled using NVO coated carbon cloth as the cathodes with a size of 7*5 cm, zinc metal foils with a size of 7*5 cm as the anodes, and BN-PAN or PAN membranes with a size of 8*6 cm as separators. The coating area of NVO active materials was 5*5 cm. These components were then vacuum-encapsulated into aluminum plastic film-sealed bags.

In the GITT test, batteries were charged and discharged for 10 min at the current density of 100 mA g^{-1}, followed with an open circuit step for 60 min to relax back to equilibrium. The Zn-ion diffusion coefficients ($D_{Zn^{2+}}$) was calculated by using the following equation.

$$D_{Zn^{2+}}^{GITT} = \frac{4}{\pi \cdot \tau}\left(\frac{n_m V_m}{S}\right)^2\left(\frac{\Delta E_s}{\Delta E_t}\right)^2 \quad (1)$$

Where, τ is the current pulse duration (10 min); n_m is the quantity of moles; V_m is the molar volume; *S* is the interface area between electrode and electrolyte (served as the geometric area of the electrode); ΔE_s and ΔE_t are the steady-state voltage change and the overall voltage change after adding a current pulse in a cycle of GITT test.

The ionic conductivities of the separators were tested by using Stainless Steel (SS) //SS cells and calculated as following equation.

$$\sigma = \frac{l}{R \cdot S} \quad (2)$$

Where, l represents the thickness of the separator; R represents the resistance measured in EIS test; S represents the contact area between stainless steel electrode and the separator.

The activation energy (Ea) of the separators was evaluated by Zn symmetric batteries and calculated by using the Arrhenius equation.

$$\frac{1}{R_{ct}} = \mathrm{A}e^{-\frac{E_a}{RT}} \tag{3}$$

where R_{ct} represents the charge transfer resistance, A represents frequency factor, R represents gas constant, T represents absolute temperature.

The Zn^{2+} transference number ($t_{Zn^{2+}}$) of the separators are measured by using Zn symmetric batteries based on the following equation.

$$t_{Zn^{2+}} = \frac{I_s(\Delta \mathrm{V} - I_0 R_0)}{I_0(\Delta \mathrm{V} - I_s R_s)} \tag{4}$$

Where, ΔV is the constant polarization voltage (10 mV); I_0 and I_s are the initial current and the stable current respectively; R_0 and R_s are the initial resistance and the stable resistance respectively.

***In situ* FTIR measurement.** *In situ* FTIR measurements were conducted in ATR mode using Zn//Ti cell, where Ti mesh and zinc foil served as the cathode and anode, respectively, with BN-PAN or PAN membrane as the separator. In the process of collecting spectra, the infrared beam firstly passed through the silicon crystal to reach the sample and then the reflected infrared beam was ejected from the cell. Finally, the infrared beam would be detected by the detector and further analyzed. The initial infrared spectrum was

collected as the background, and subsequent spectra were processed to obtain corresponding operational signals.

***In situ* optical microscope measurement.** The tailor-made electrochemical cell for *in situ* optical microscope measurement was purchased from Beijing Scistar Technology Co., Ltd. The cell was assembled with two Zn anodes and different separators cycled at the current of 5.0 mA on the LAND battery test system. The test temperature is constant at 25 °C. The cross-section of the anode was observed on the optical microscope (Olympus U-MSSP).

Simulation of ion diffusion. The ion diffusion on the zinc anode was predicted by Nernst-Planck formulation. The modeling domain, geometrical dimensions and major boundary conditions were shown in Fig. 3e and 3f. The length of the electrode is 6 μm, and the protrusion structures of zinc anode are designed as semicircles with a radius of 0.3 μm. The thickness of the separator and electrolyte is 2.5 μm. The governing equations are given as follows.

$$\nabla \cdot \boldsymbol{J_i} + \boldsymbol{u} \cdot \nabla c_i = R_i \tag{5}$$

$$\nabla \cdot i_l = F \sum_i z_i R_i \tag{6}$$

$$\boldsymbol{J_i} = -D_i \nabla c_i - z_i \boldsymbol{u}_{m,i} F c_i \nabla V + \boldsymbol{u} c_i \tag{7}$$

Where, $\boldsymbol{J_i}$ is the mass flux for each species; D_i is the diffusion coefficient (3.36×10^{-5} cm^2 s for Zn^{2+} and 1.38×10^{-5} cm^2 s for SO_4^{2-}); c_i is the concentration; z_i is the charge number (2 for Zn^{2+} and -2 for SO_4^{2-}); ∇V is the electrolyte potential; F is Faraday constant.

$\boldsymbol{u}$ is set to be 0 as convection is not considered in the process. It is assumed that the entire field is electrically neutral. The boundary conditions are defined that the experimentally determined polarization voltage of the symmetric cell is specified as the cathodic potential, while the anodic potential is held at a constant value of 0 and the Zn^{2+} concentration on the anodic surface is determined to be 2 M. The experimental current is 0.5 mA cm^{-2}. The model was solved in the solver COMSOL Multiphysics with fully coupled Newton method.

Computational methods. ORCA version 5.0.2 was used for all DFT calculation where B3LYP functional with DEF2-SVP basis set was used to consider the exchange and correlation effects between the electrons.[1, 2] The def2/J auxiliary basis set and RIJCOSX algorithm were used to accelerate the DFT caculation.[3, 4] The conductor-like polarizable continuum model (CPCM) was employed to consider the solvation effect for aqueous systems.[5] All structures were fully relaxed in the optimization until the force was less than 3×10^{-4} Eh $bohr^{-1}$ with a self-consistent field convergence criterion of 5×10^{-6} Eh. To estimate the transition state (TS) of the migration of the Zn^{2+} and obtain the diffusion energies, A combination of the Nudged Elastic Band and Saddle Point Optimization (NEB-TS) with the Image Dependent Pair Potential (IDPP) method was operated.[6, 7] Meanwhile, the vibrational analysis was performed to verify the correctness of the TS. The DFT caculation results were visualized by the VESTA software.[8]

2. Supporting Figures

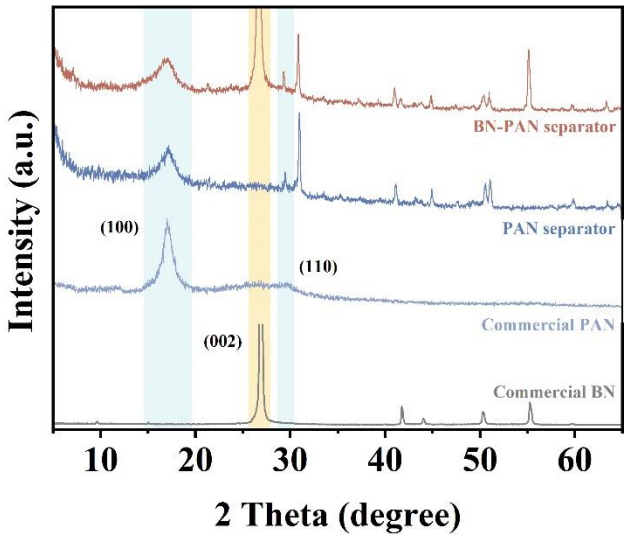

Fig. S1. XRD patterns of BN-PAN separator, PAN separator, commercial PAN powder and commercial BN powder.

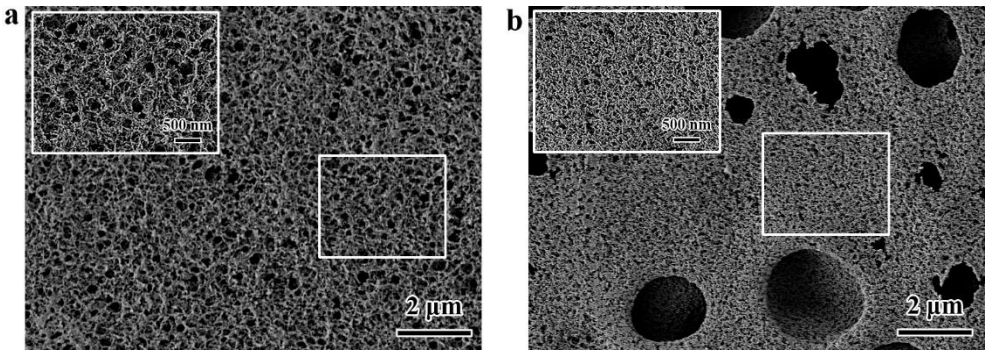

Fig. S2. SEM images of a) BN-PAN separator and b) PAN separator.

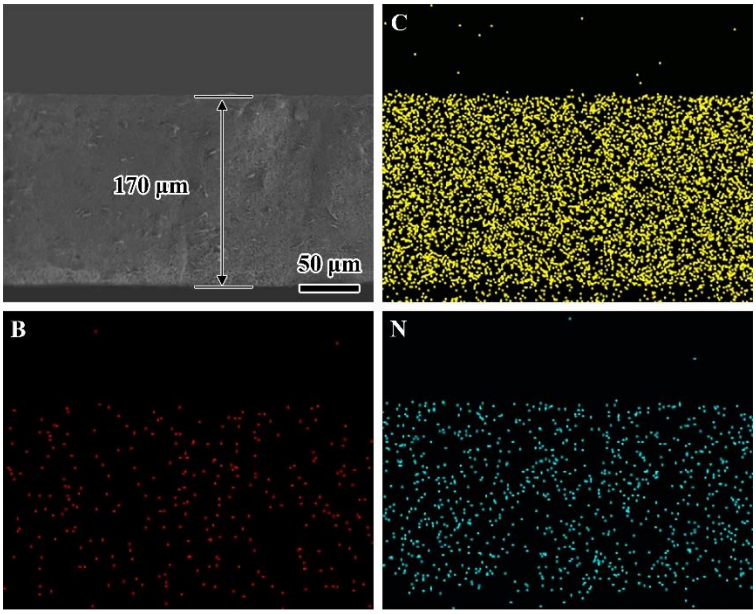

Fig. S3. Cross-sectional SEM image and corresponding EDS elemental mappings of BN-PAN separator.

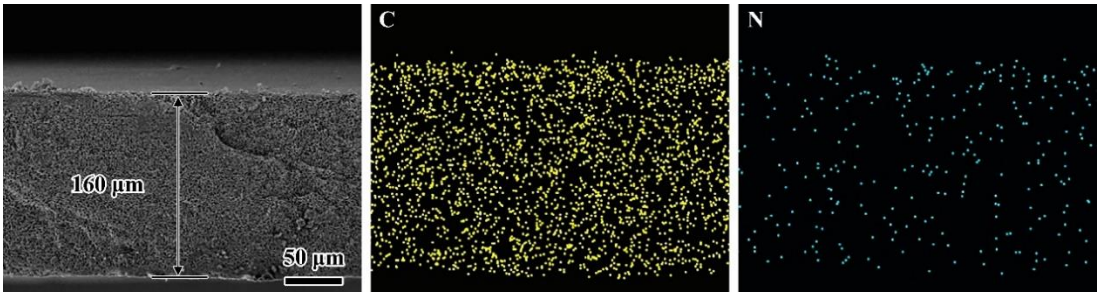

Fig. S4. Cross-sectional SEM image and corresponding EDS elemental mappings of PAN separator.

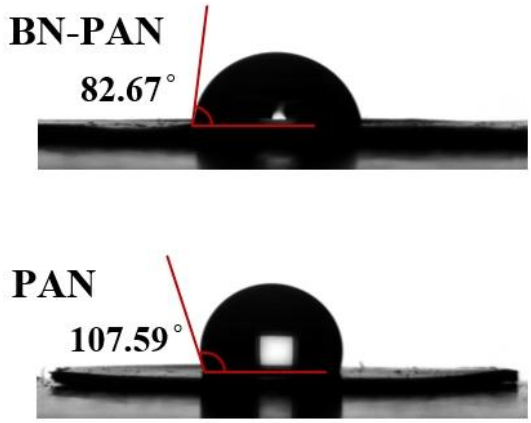

Fig. S5. Contact angle test of BN-PAN separator and PAN separator respectively.

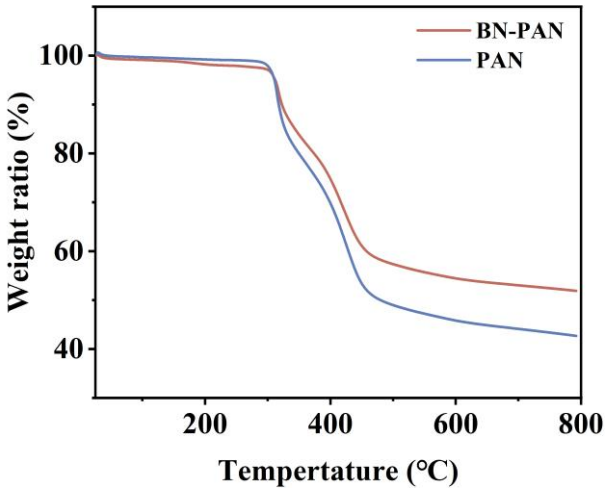

Fig. S6. The thermogravimetric analysis of BN-PAN and PAN separator.

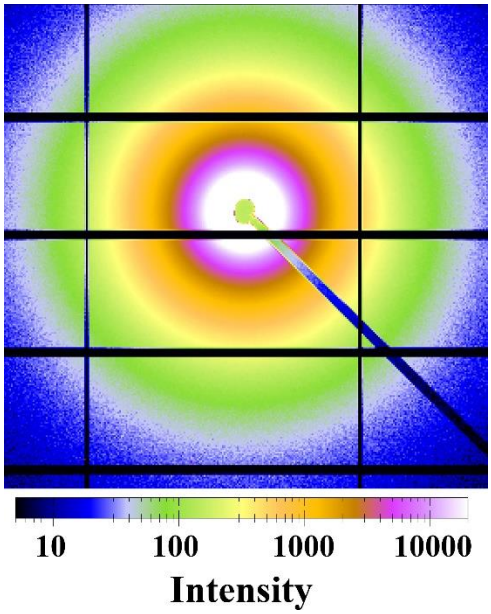

Fig. S7. 2D SR-SAXS pattern of PAN separator.

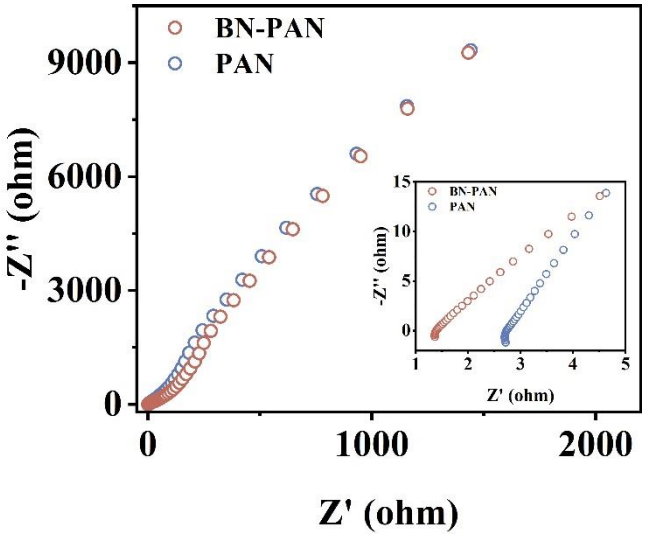

Fig. S8. Electrochemical impedance spectroscopy (EIS) of SS//SS cells with BN-PAN separator and PAN separator.

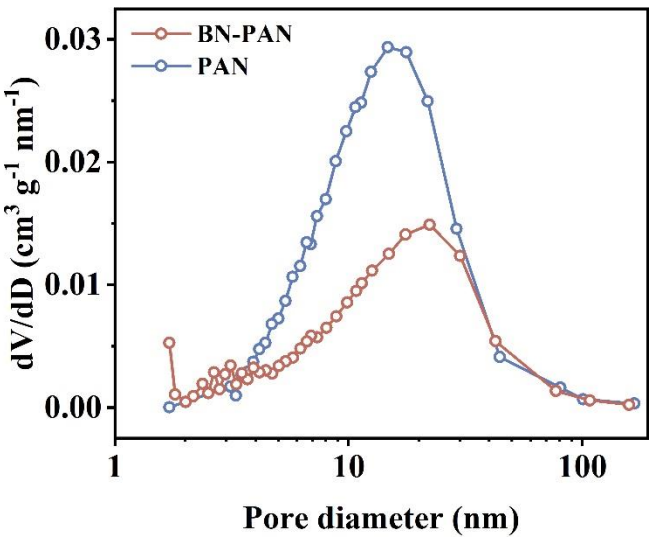

Fig. S9. BJH adsorption-desorption pore distribution of BN-PAN separator and PAN separator.

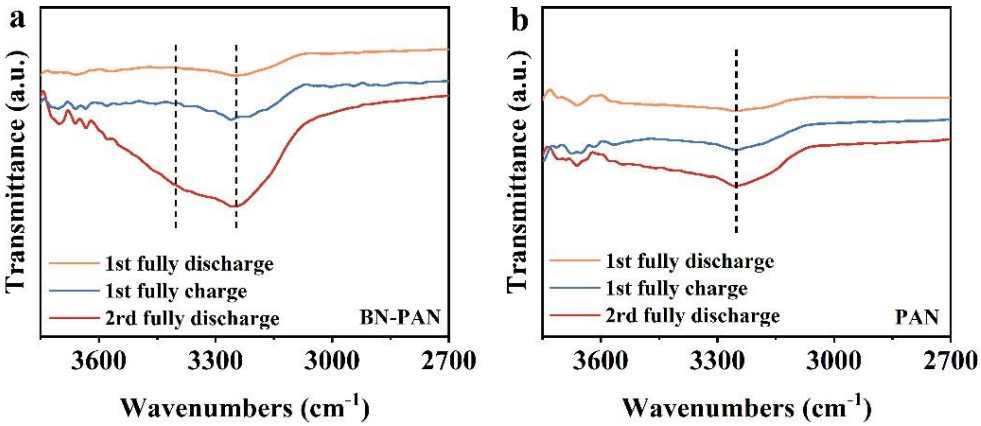

Fig. S10. FTIR spectra of fully discharged and charged state of Zn//Ti cells with a) BN-PAN separator and b) PAN separator from the *in situ* FTIR results.

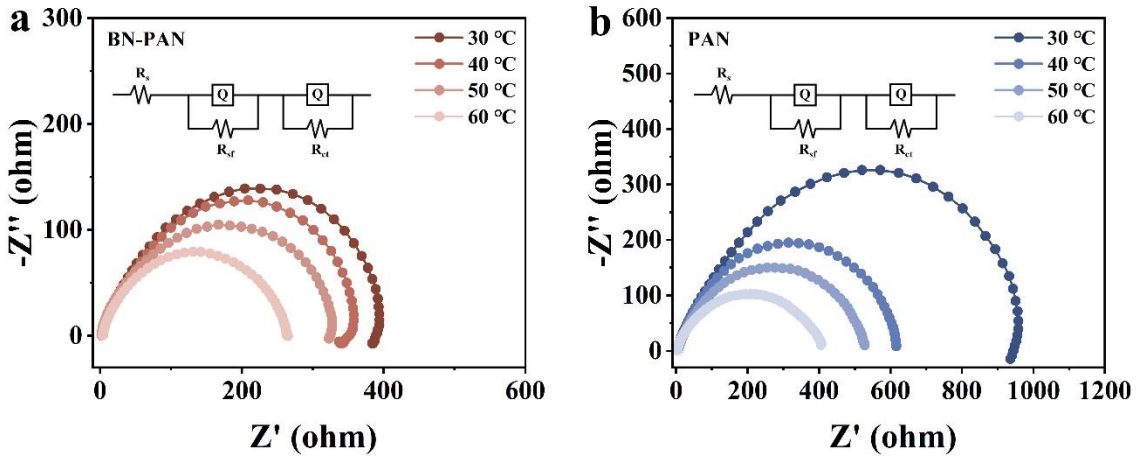

Fig. S11. EIS of Zn//Zn cells with a) BN-PAN separator and b) PAN separator at different temperatures.

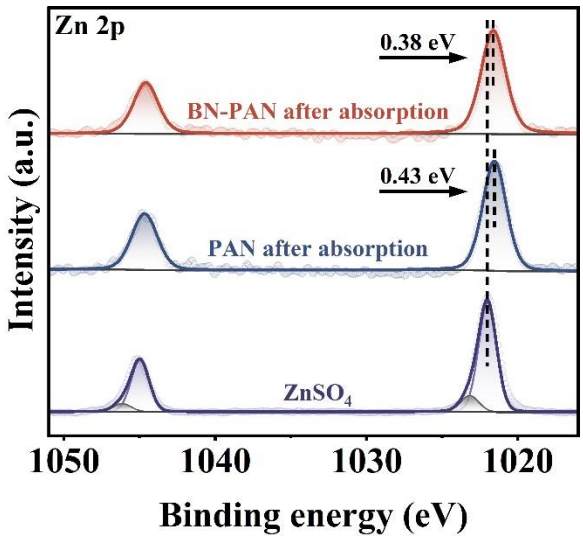

Fig. S12. XPS spectra of Zn 2p spectrum of BN-PAN separator and PAN separator after adsorption in 2 M $ZnSO_4$ and pure $ZnSO_4$ salt.

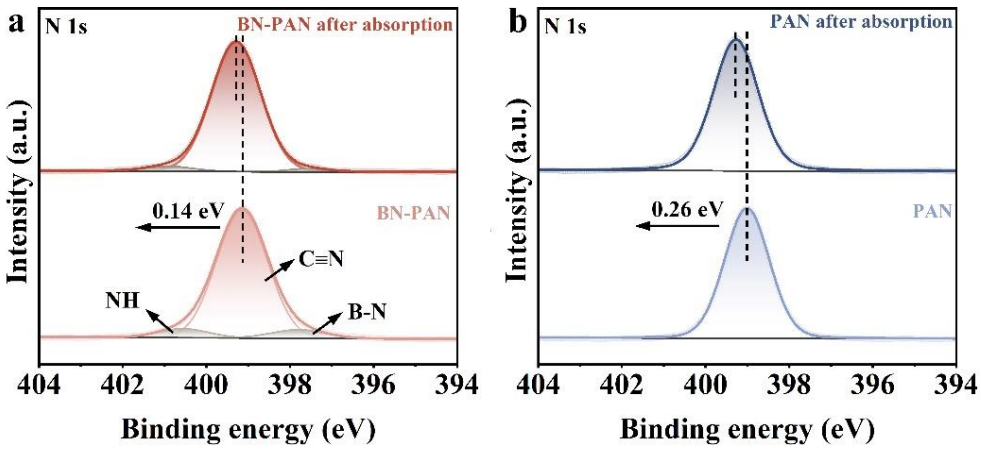

Fig. S13. XPS spectra of N 1s spectrum of BN-PAN separator and PAN separator after adsorption in 2 M $ZnSO_4$.

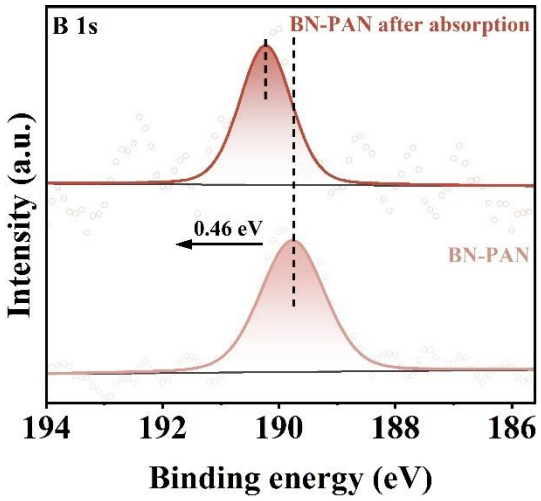

Fig. S14. XPS spectra of B 1s spectrum of the BN-PAN separator after immersion in 2 M $ZnSO_4$ electrolyte for 2 days.

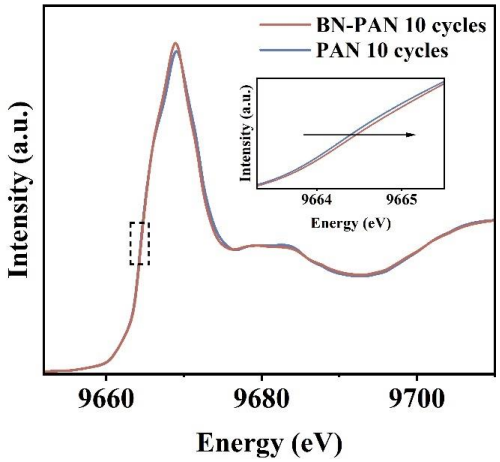

Fig. S15. Zn K-edge XANES spectra of BN-PAN and PAN separators after 10 cycles.

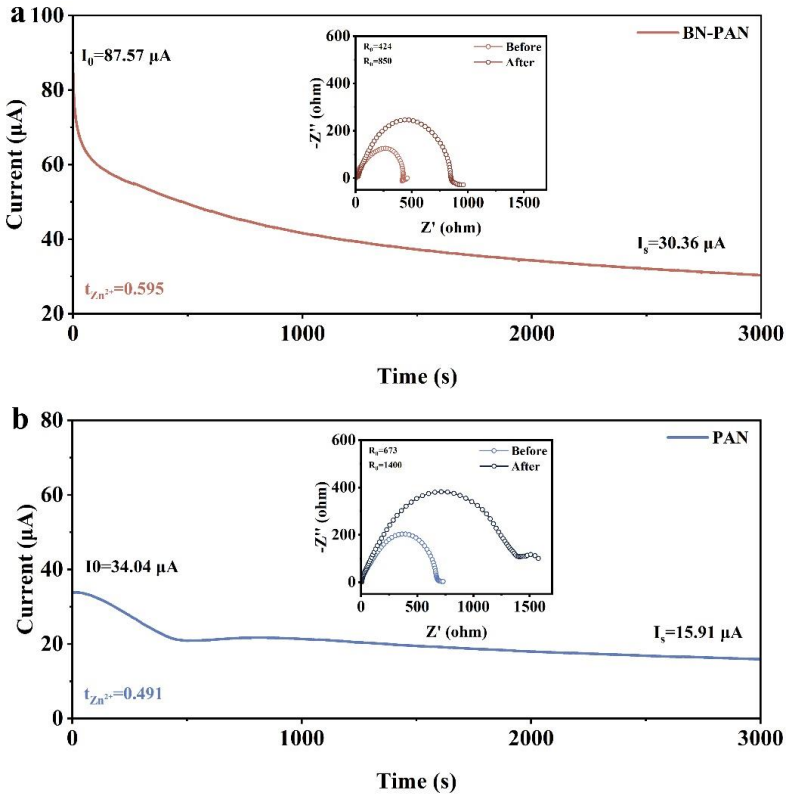

Fig. S16. Zn^{2+} transference number calculated by current-time plot at a constant potential of 10 mV and EIS spectra before and after polarization in Zn symmetric cell based on a) BN-PAN separator and b) PAN separator.

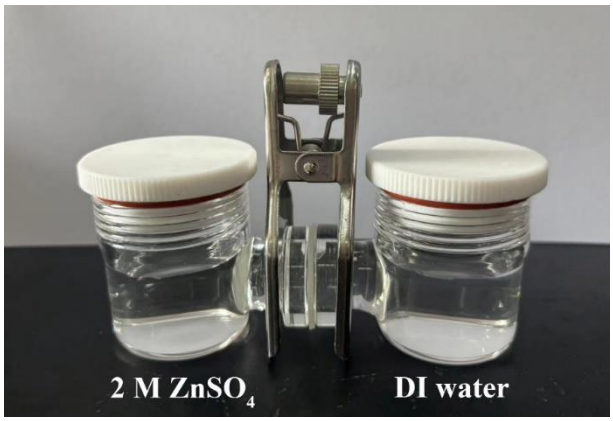

Fig. S17. The ion selectivity of BN-PAN and PAN separators tested by H-cells with 2 M $ZnSO_4$ in one side and DI water in the other side.

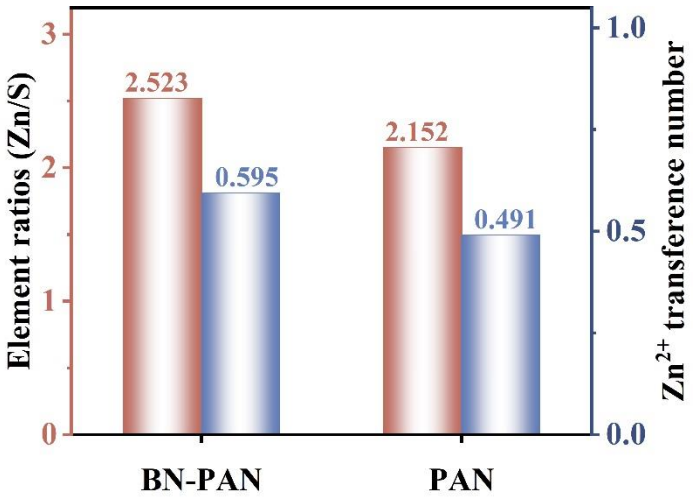

Fig. S18. Zn^{2+} transference number and Zn/S transmission ratio of BN-PAN and PAN separators.

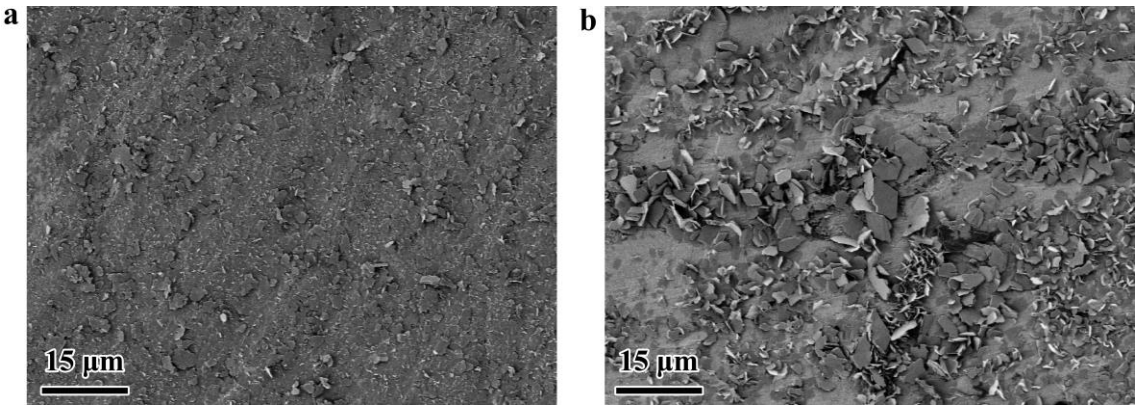

Fig. S19. The SEM images of Zn anode surface after 10 cycles with a) BN-PAN separator and b) PAN separator at a small magnification.

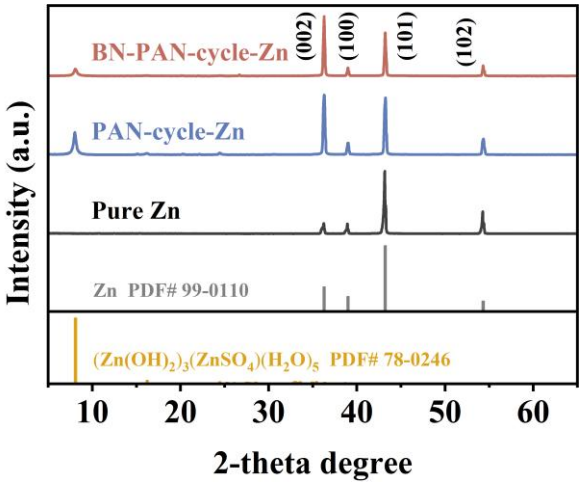

Fig. S20. XRD patterns of cycled Zn anodes.

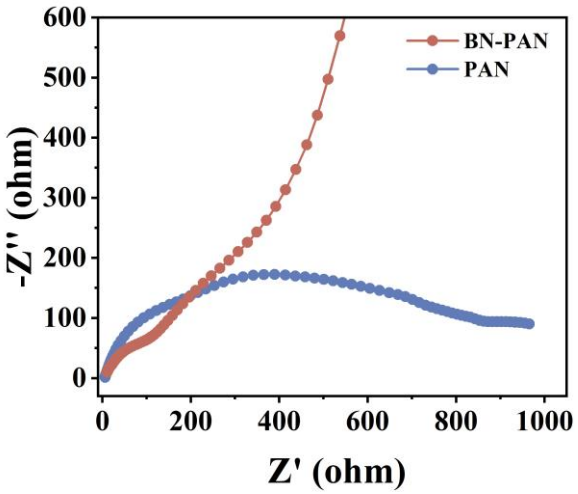

Fig. S21. EIS of Zn//Zn cells with BN-PAN separator and PAN separator after 10 cycles.

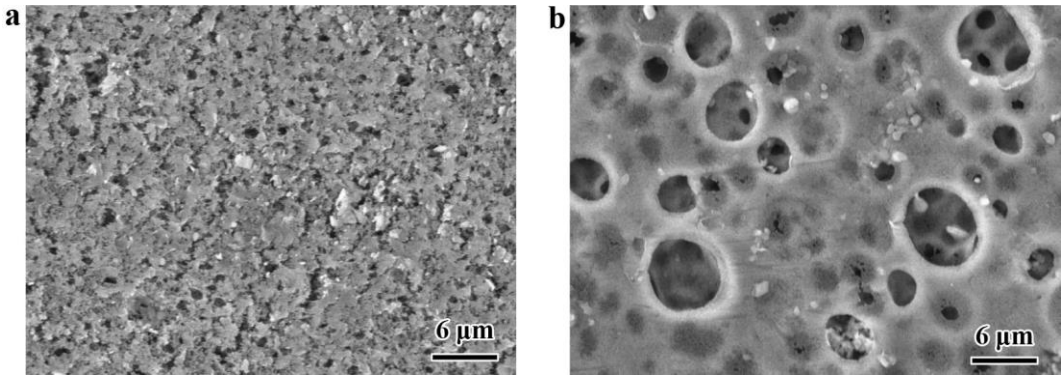

Fig.S22. The SEM images of a) BN-PAN separator and b) PAN separator after cycling for 5 cycles.

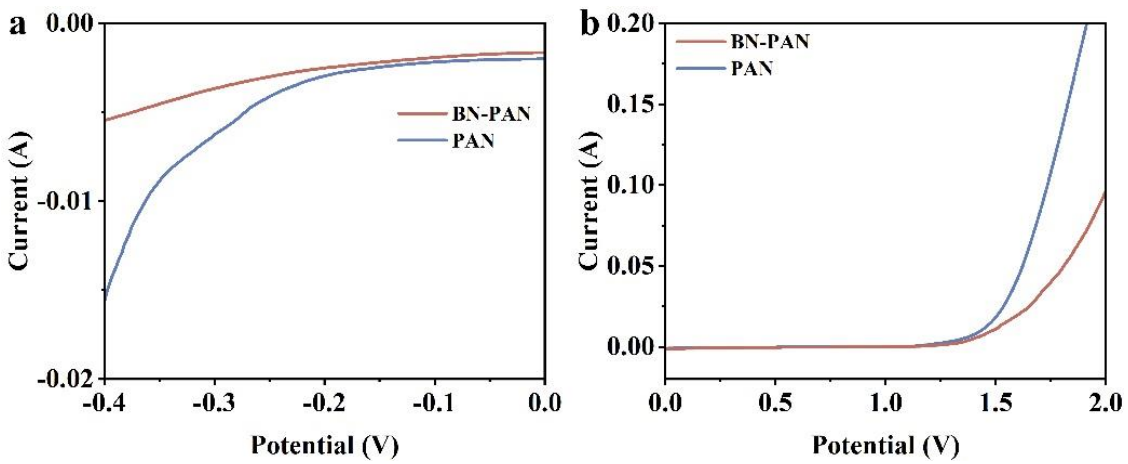

Fig. S23. The linear sweep voltammetry (LSV) curves of Zn//Cu cells with BN-PAN separator and PAN separator at 0.1 V s^{-1}.

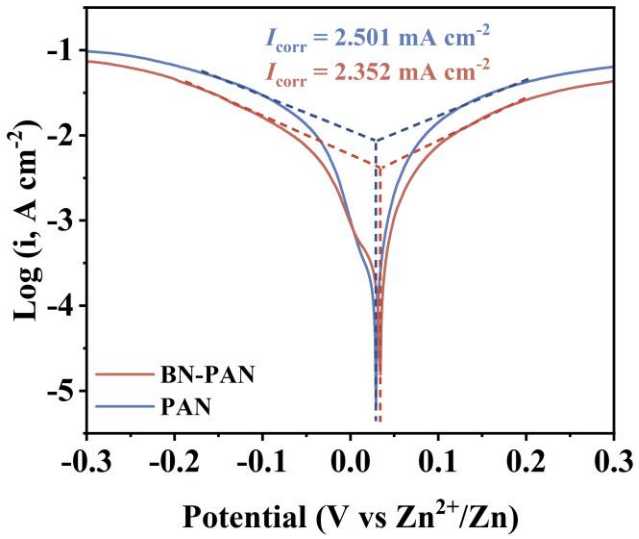

Fig. S24. The Tafel plots of Zn//Zn cells with BN-PAN separator and PAN separator at 10 mV s^{-1}.

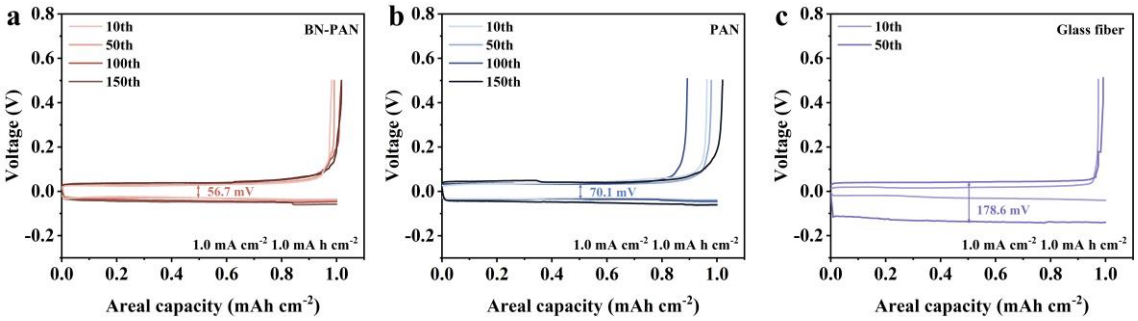

Fig. S25. Voltage profiles of Zn//Cu cells with a) BN-PAN separator, b) PAN separator and c) glass fiber separator.

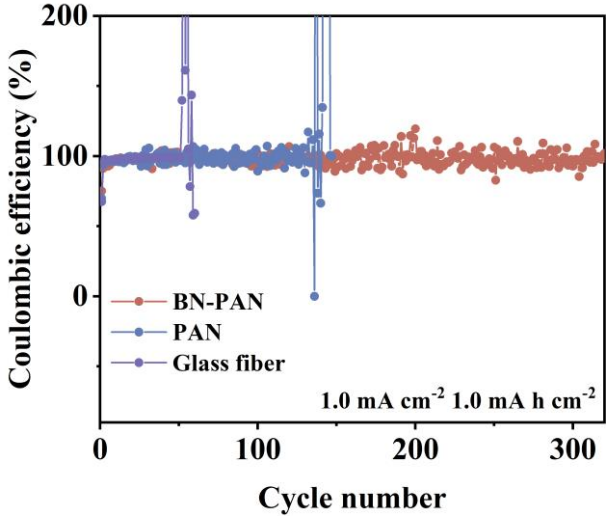

Fig. S26. Coulombic efficiencies of Zn//Cu cells with BN-PAN separator, PAN separator and glass fiber separator.

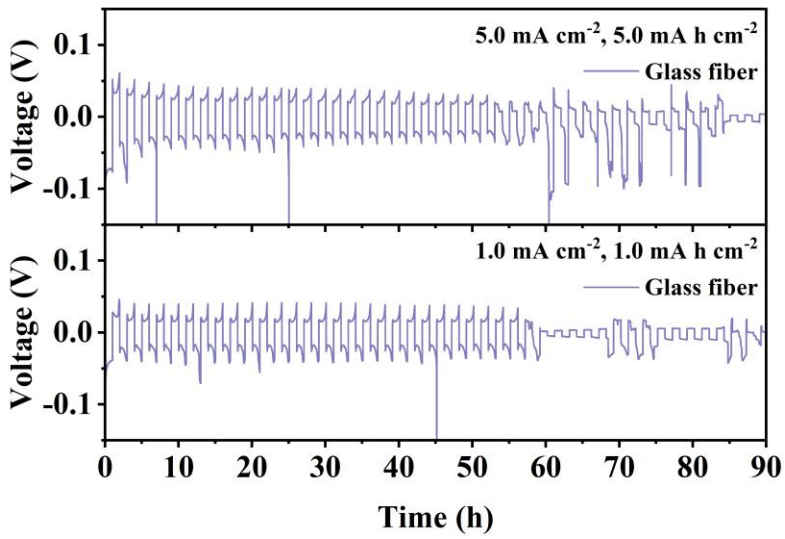

Fig. S27. The cycling performance of Zn//Zn cells at 1.0 mA cm^{-2} with 1.0 mA h cm^{-2} and 5.0 mA cm^{-2} with 5.0 mA h cm^{-2} of glass fiber separator.

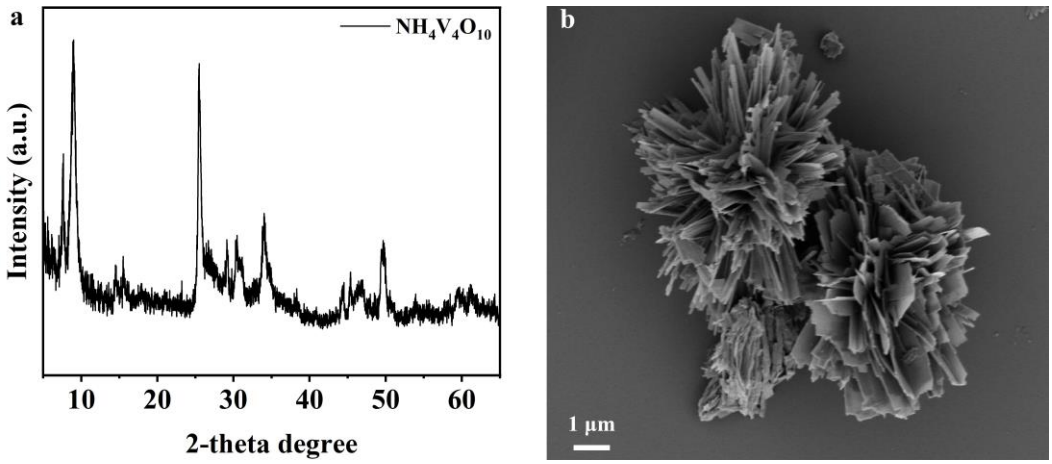

Fig. S28. a) XRD pattern and b) SEM image of $NH_4V_4O_{10}$.

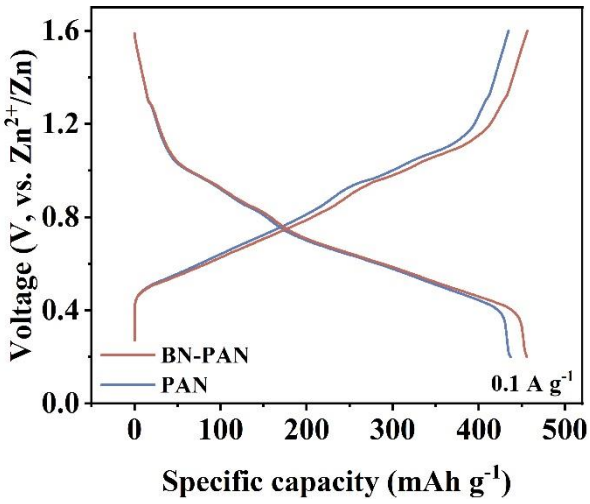

Fig. S29. The charge-discharge voltage profiles of Zn//NVO cells at the current density of 0.1 A g^{-1}.

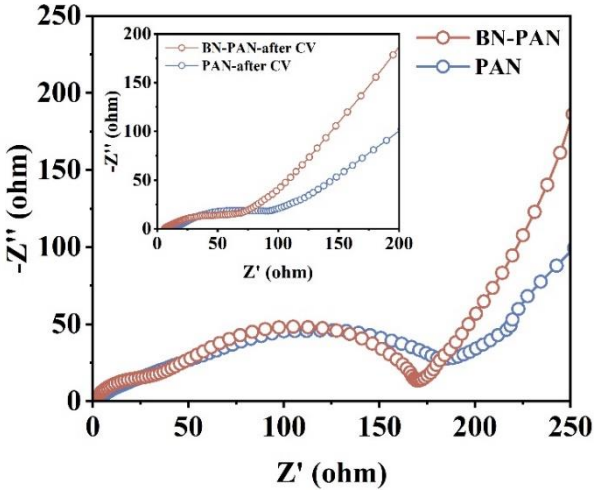

Fig. S30. EIS spectra of Zn/BN-PAN/NVO cell and Zn/PAN/NVO cell before and after CV test.

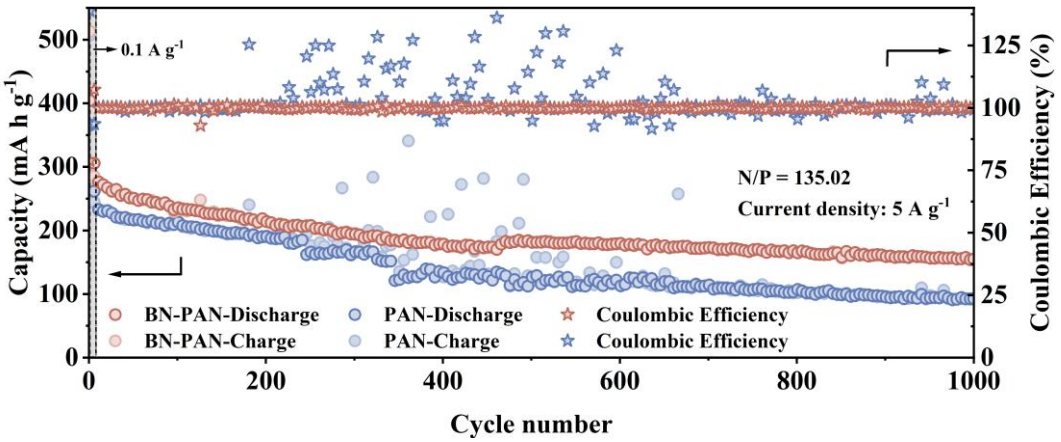

Fig. S31. The cycling stability of Zn/BN-PAN/NVO cell and Zn/PAN/NVO cell at the current density of 5.0 A g^{-1} with a N/P ratio of 135.02, including 5 cycles of pre-cycling at the low current density of 0.1 A g^{-1}.

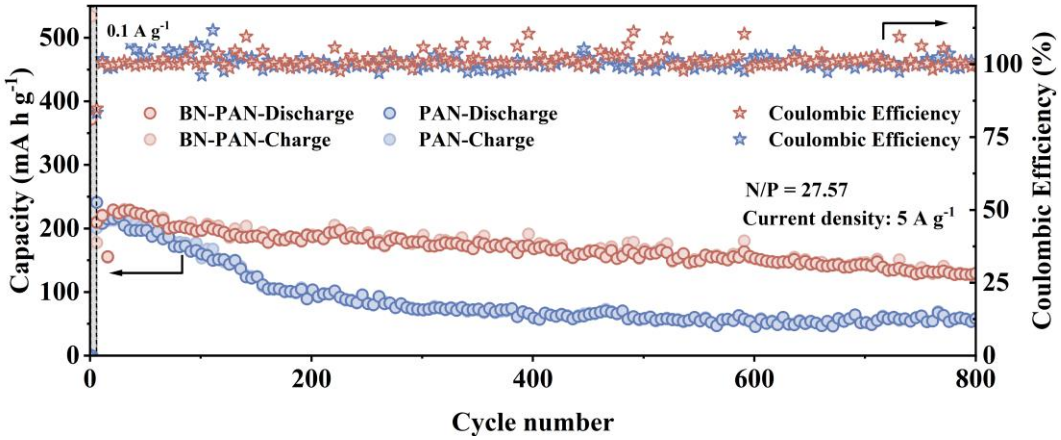

Fig. S32. The cycling stability of Zn/BN-PAN/NVO cell and Zn/PAN/NVO cell at the current density of 5.0 A g^{-1} with a N/P ratio of 27.57, including 5 cycles of pre-cycling at the low current density of 0.1 A g^{-1}.

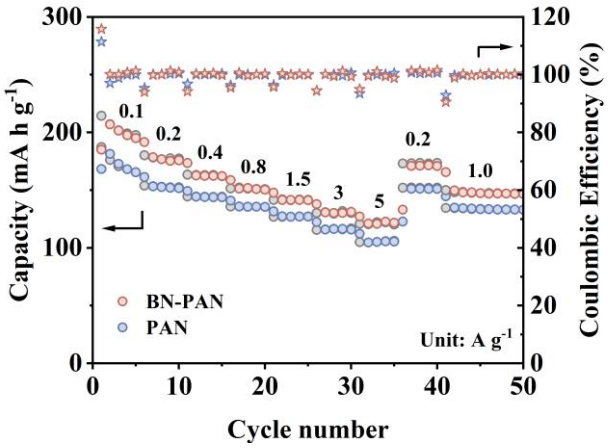

Fig. S33. The rate performance of Zn-I_2 batteries with BN-PAN and PAN separator at the current density from 0.1 A g^{-1} to 5.0 A g^{-1}.

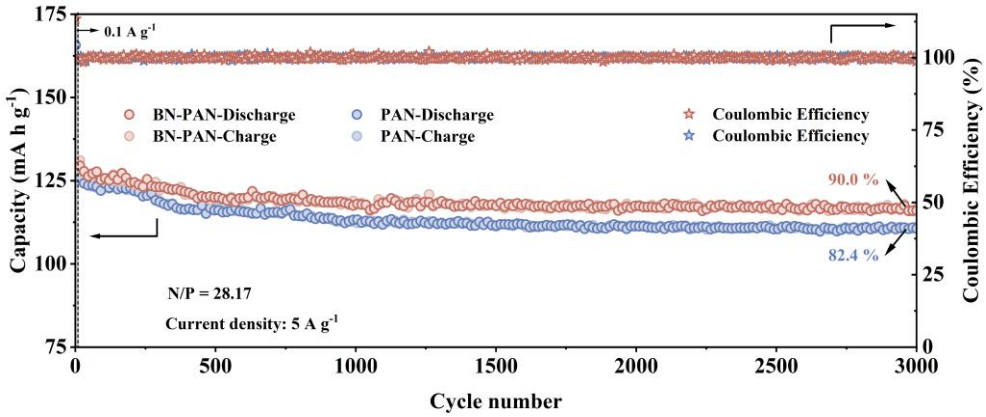

Fig. S34. The cycling stability of Zn-I_2 batteries with BN-PAN and PAN separator at the current density of 5.0 A g^{-1} with a N/P ratio of 28.17, including 5 cycles of pre-cycling at the low current density of 0.1 A g^{-1}.

3. Supporting Tables

Table S1. Imaginary frequency verification of transition states for BN given in calculations.

Number	Vibrational frequencies (cm^{-1})	Number	Vibrational frequencies (cm^{-1})	Number	Vibrational frequencies (cm^{-1})
0	0.00	45	638.70	90	1165.95
1	0.00	46	651.16	91	1168.48
2	0.00	47	652.95	92	1204.28
3	0.00	48	657.78	93	1205.73
4	0.00	49	661.31	94	1244.21
5	0.00	50	678.22	95	1251.13
6	-58.66 Imaginary mode	51	690.22	96	1260.27
7	32.74	52	696.74	97	1264.79
8	55.11	53	699.93	98	1272.79
9	79.90	54	706.20	99	1275.97
10	87.79	55	717.42	100	1278.60
11	93.10	56	723.30	101	1287.62
12	100.02	57	728.00	102	1297.83
13	141.51	58	728.99	103	1316.85
14	158.65	59	741.32	104	1326.27

15	181.11	60	743.33	105	1348.46
16	191.20	61	765.63	106	1357.08
17	208.88	62	779.82	107	1369.86
18	221.43	63	785.94	108	1374.59
19	223.37	64	795.98	109	1390.43
20	244.75	65	810.86	110	1406.27
21	256.44	66	893.03	111	1410.33
22	281.18	67	895.77	112	1425.75
23	291.56	68	908.79	113	1435.40
24	301.21	69	917.51	114	1438.85
25	322.41	70	921.23	115	1464.45
26	335.92	71	922.24	116	1468.54
27	337.83	72	936.68	117	1478.41
28	361.09	73	937.91	118	1515.02
29	366.72	74	955.51	119	1519.16
30	368.03	75	959.25	120	1529.69
31	376.82	76	973.30	121	2599.24
32	379.36	77	986.98	122	2611.03
33	383.90	78	1014.26	123	2615.78
34	406.86	79	1028.30	124	2621.37

35	438.29	80	1043.74	125	2625.80
36	443.85	81	1061.53	126	2634.46
37	497.01	82	1065.83	127	2639.95
38	506.75	83	1068.36	128	3576.80
39	540.62	84	1082.70	129	3581.68
40	550.96	85	1093.35	130	3584.37
41	557.00	86	1116.93	131	3596.68
42	584.07	87	1136.19	132	3602.30
43	588.05	88	1148.96	133	3602.98
44	617.54	89	1161.19	134	3606.59

Table S2. Imaginary frequency verification of transition states for PAN given in calculations.

Number	Vibrational frequencies (cm^{-1})	Number	Vibrational frequencies (cm^{-1})	Number	Vibrational frequencies (cm^{-1})
0	0.00	52	574.66	104	1340.81
1	0.00	53	576.78	105	1350.64
2	0.00	54	580.24	106	1361.35
3	0.00	55	588.51	107	1366.03
4	0.00	56	595.60	108	1368.77

5	0.00	57	623.27	109	1374.02
6	-80.46 Imaginary mode	58	659.56	110	1376.25
7	11.35	59	686.12	111	1383.82
8	18.47	60	713.57	112	1386.95
9	20.32	61	740.00	113	1390.81
10	30.19	62	761.83	114	1393.08
11	32.78	63	784.78	115	1393.75
12	37.08	64	808.71	116	1400.81
13	46.21	65	813.29	117	1417.62
14	53.89	66	839.70	118	1439.18
15	60.84	67	858.08	119	1442.64
16	72.18	68	870.72	120	1447.73
17	80.18	69	886.88	121	1449.21
18	93.04	70	893.92	122	1449.89
19	95.92	71	913.90	123	1456.81
20	103.04	72	920.96	124	1457.75
21	106.37	73	944.71	125	1469.26
22	114.38	74	966.38	126	2356.80
23	133.26	75	992.88	127	2358.33
24	148.08	76	1002.78	128	2362.03

25	157.13	77	1020.40	129	2362.60
26	162.67	78	1027.28	130	2362.92
27	187.22	79	1029.93	131	2368.32
28	197.38	80	1049.21	132	2403.84
29	203.38	81	1059.41	133	3039.05
30	217.83	82	1080.37	134	3039.49
31	233.82	83	1087.25	135	3041.89
32	244.13	84	1093.90	136	3045.75
33	245.60	85	1105.00	137	3047.70
34	263.30	86	1113.77	138	3048.32
35	271.96	87	1120.30	139	3048.37
36	284.31	88	1133.39	140	3053.88
37	295.97	89	1139.07	141	3063.92
38	297.23	90	1196.83	142	3064.79
39	311.78	91	1200.46	143	3068.71
40	317.85	92	1223.63	144	3078.55
41	328.29	93	1226.25	145	3082.38
42	364.47	94	1228.61	146	3091.71
43	370.30	95	1241.91	147	3105.66
44	393.66	96	1247.47	148	3117.31

45	420.43	97	1266.76	149	3120.60
46	435.02	98	1277.92	150	3131.19
47	460.12	99	1288.08	151	3131.79
48	546.69	100	1299.71	152	3132.84
49	552.68	101	1305.39	153	3137.74
50	561.53	102	1314.83	154	3146.05
51	569.54	103	1333.65	155	3153.34

Table S3. DFT calculation results for the structure of BN and PAN after the absorption of zinc ions.

	Average bond length (Å)
Zn-N bond in PAN	2.093
Zn-N bond in BN	2.063

Table S4. The comparison based on cycling life of modified separators among BN-PAN separator and previous reports.

Separator materials	**Current density (mA cm^{-2})**	**Areal capacity (mA h cm^{-2})**	**Cycling life (h)**	**References**
CNF+LMS	5	2.5	500	Ref. [9]
	1	0.5	1000	
BPDA|PE|BisSF	1	1	1000	Ref. [10]
	5	5	500	

Zn-Nafion	5	0.5	553	Ref. [11]
GF@SM	5	3	250	Ref. [12]
BC membrane	5	5	300	Ref. [13]
PAN	0.283	0.283	800	Ref. [14]
SPSF@PMIA	1	1	1000	Ref. [15]
	5	2.5	550	
Zn@C_3N_4@GF	0.1	0.1	400	Ref. [16]
PAN-S	0.5	1	350	Ref. [17]
Zn-BTC	2	2	700	Ref. [18]
	5	2.5	350	
GF/PBPT	2	2	600	Ref. [19]
CS-filter paper	5	1	450	Ref. [20]
BN-PAN	0.5	0.5	2100	**This work**
	1.0	1.0	1100	
	5.0	5.0	720	

Table S5. The N/P ratio of Zn//NVO full cells.

Zn thickness (μm)	Negative capacity (mAh)	Positive capacity (mAh)	N/P ratio
30	19.85	0.72	27.57
100	66.16	0.49	135.02

Table S6. The comparison of the electrochemical performance in full batteries among BN-PAN separator and previous reports.

Separator	Cathode	Current density	Capacity (mA h g^{-1})	Electrolyte	References
Titanium Nitride-Cellulose Nanofiber [21]	$(NH_4)_2V_{10}O_{25}$	5 A g^{-1}	200.0	2 M $ZnSO_4$	*ACS Appl. Energy Mater.*, 2024, 7, 17, 7496.
Fly ash-cellulose separator [22]	$(NH_4)_2V_{10}O_{25}$	5 A g^{-1}	177.8	2 M $ZnSO_4$	*Small.*, 2024, 20, 2311203.
polydopamine-functionalized PVDF nanofibrous membrane [23]	$NH_4V_4O_{10}$	5 A g^{-1}	215.1	3 M $ZnSO_4$	*InfoMat.*, 2023, 5, e12374.
Polyacrylonitrile nanofiber separator [14]	$NH_4V_4O_{10}$	5 A g^{-1}	195.5	2 M $ZnSO_4$	*Adv. Funct. Mater.*, 2022, 32, 2109671.
Oxygen-functionalized biomass bamboo membrane separator [24]	$NaV_3O_8 \cdot 1.5H_2O$	5 A g^{-1}	192.8	1 M $Zn(OTf)_2$	*Adv. Mater.*, 2024, 36, 2406429.

Mesoporous FE Al_2O_3/P(VDF-TrFE) membrane [25]	$NaV_3O_8 \cdot 1.5H_2O$	0.2 A g^{-1}	298.0	1 M $ZnSO_4$+0.1M Na_2SO_4	*Nano Lett.*, 2024, 24, 16, 4785.
CA@DF separator [26]	V_2O_5	5 A g^{-1}	100.68	2 M $ZnSO_4$	*Chem. Eng. J.*, 2024, 479, 147846.
BPDA|PE|BisSF separator [10]	V_2O_5	5 A g^{-1}	53.0	2 M $ZnSO_4$	*Adv. Funct. Mater.*, 2024, 34, 2400959.
CNF+LMS separator [9]	VO_2	5 A g^{-1}	176.0	2 M $ZnSO_4$	*Chem. Eng. J.*, 2024, 480, 147980.
Zn@C_3N_4@GF separator [16]	$Zn_3V_3O_8$@CN	3 A g^{-1}	222.5	3 M $Zn(CF_3SO_3)_2$	*Chem. Eng. J.*, 2024, 486, 150377.
Zn-BTC membrane [18]	Ketjenblack with 0.5 M $ZnSO_4$, 1 M LiI and 0.1 M I_2	1.28 A g^{-1}	102.6	0.5 M $ZnSO_4$ + 0.5 M Li_2SO_4	*Adv. Mater.*, 2020, 32, 2004240.
Zeolite Membrane Separator [27]	Ketjenblack with 0.5 M $ZnSO_4$, 1 M LiI and 0.1 M I_2	4 A g^{-1}	47.8	0.5 M $ZnSO_4$ + 0.5 M Li_2SO_4	*Nano Lett.*, 2022, 22, 6, 2538.
Modified cotton fiber separator [28]	I_2/MCN	0.5 A g^{-1}	114	1 M $ZnSO_4$	*Colloids Surf., A.*, 2024, 684, 133239.
ODGelMA [29]	I_2	5 C	109.2	1 M $ZnSO_4$	*Adv. Mater.*, 2024, 36, 2403214.
PC-PVA/$Zn(CF_3SO_3)_2$ gel electrolyte [30]	I_2/CNTs	1 A g^{-1}	120.1	1 M $Zn(CF_3SO_3)_2$	*Energy Storage Mater.*, 2025, 74, 103981.
BN-PAN separator	$NH_4V_4O_{10}$	5 A g^{-1}	222.3	2 M $ZnSO_4$	**This work**
	I_2/active carbon	5 A g^{-1}	121.2	2 M $ZnSO_4$	

REFERENCES

1. A. D. Becke, Density-functional thermochemistry. III. The role of exact exchange, *J. Chem. Phys.*, 1993, **98**, 5648-5652.
2. F. Weigend and R. Ahlrichs, Balanced basis sets of split valence, triple zeta valence and quadruple zeta valence quality for H to Rn: Design and assessment of accuracy, *Phys. Chem. Chem. Phys.*, 2005, **7**, 3297-3305.
3. F. Weigend, Accurate Coulomb-fitting basis sets for H to Rn, *Phys. Chem. Chem. Phys.*, 2006, **8**, 1057-1065.
4. F. Neese, F. Wennmohs, A. Hansen and U. Becker, Efficient, approximate and parallel Hartree–Fock and hybrid DFT calculations. A 'chain-of-spheres' algorithm for the Hartree–Fock exchange, *Chem. Phys.*, 2009, **356**, 98-109.
5. V. Barone and M. Cossi, Quantum Calculation of Molecular Energies and Energy Gradients in Solution by a Conductor Solvent Model, *J. Phys. Chem. A.*, 1998, **102**, 1995-2001.
6. V. Ásgeirsson, B. O. Birgisson, R. Bjornsson, U. Becker, F. Neese, C. Riplinger and H. Jónsson, Nudged Elastic Band Method for Molecular Reactions Using Energy-Weighted Springs Combined with Eigenvector Following, *J. Chem. Theory Comput.*, 2021, **17**, 4929-4945.
7. S. Smidstrup, A. Pedersen, K. Stokbro and H. Jónsson, Improved initial guess for minimum energy path calculations, *J. Chem. Phys.*, 2014, **140**, 214106.
8. K. Momma and F. Izumi, VESTA 3 for three-dimensional visualization of crystal, volumetric and morphology data, *J. Appl. Crystallogr.*, 2011, **44**, 1272-1276.
9. J. Cao, D. Zhang, R. Chanajaree, D. Luo, X. Yang, X. Zhang and J. Qin, A low-cost separator enables a highly stable zinc anode by accelerating the de-solvation effect, *Chem. Eng. J.*, 2024, **480**, 147980.
10. R. Xue, Z. Wang, N. Yao, Y. Liu, H. Wang, M. Zhang, A. Shao, X. Tang, J. Liu, J. Tang, Z. Wang and Y. Ma, Multiscale Interfacial Regulation of Zn-V_2O_5 Pouch Cell via Ultrathin Molecular-Engineered Separator, *Adv. Funct. Mater.*, 2024, **34**, 2400959.

11. B. Wu, Y. Wu, Z. Lu, J. Zhang, N. Han, Y. Wang, X.-m. Li, M. Lin and L. Zeng, A cation selective separator induced cathode protective layer and regulated zinc deposition for zinc ion batteries, *J. Mater. Chem. A*, 2021, **9**, 4734-4743.

12. T. Liu, J. Hong, J. Wang, Y. Xu and Y. Wang, Uniform distribution of zinc ions achieved by functional supramolecules for stable zinc metal anode with long cycling lifespan, *Energy Storage Mater.*, 2022, **45**, 1074-1083.

13. X. Yang, Z. Zhang, M. Wu, Z.-P. Guo and Z.-J. Zheng, Reshaping Zinc Plating/Stripping Behavior by Interfacial Water Bonding for High-Utilization-Rate Zinc Batteries, *Adv. Mater.*, 2023, **35**, 2303550.

14. Y. Fang, X. Xie, B. Zhang, Y. Chai, B. Lu, M. Liu, J. Zhou and S. Liang, Regulating Zinc Deposition Behaviors by the Conditioner of PAN Separator for Zinc-Ion Batteries, *Adv. Funct. Mater.*, 2022, **32**, 2109671.

15. W. Hu, J. Ju, Y. Zhang, W. Tan, N. Deng, W. Liu, W. Kang and B. Cheng, Deposition behavior regulated by an SPSF@PMIA nanofiber separator for high-performance zinc ion batteries, *J. Mater. Chem. A*, 2022, **10**, 24761-24771.

16. R. Sun, P. Xia, X. Guo, S. Dong, F. Xu, Y. Zhang, S. Lu, Q. Zheng and H. Fan, Ternary $Zn_3V_3O_8$ superstructure and synergistic modification of separator promote high performance and stable zinc ion battery, *Chem. Eng. J.*, 2024, **486**, 150377.

17. B.-S. Lee, S. Cui, X. Xing, H. Liu, X. Yue, V. Petrova, H.-D. Lim, R. Chen and P. Liu, Dendrite Suppression Membranes for Rechargeable Zinc Batteries, *ACS Appl. Mater. Interfaces*, 2018, **10**, 38928-38935.

18. H. Yang, Y. Qiao, Z. Chang, H. Deng, P. He and H. Zhou, A Metal–Organic Framework as a Multifunctional Ionic Sieve Membrane for Long-Life Aqueous Zinc–Iodide Batteries, *Adv. Mater.*, 2020, **32**, 2004240.

19. X. Liu, W. Wei, Y. Yang, Y. Li, Y. Li, S. Xu, Y. Dong and R. He, A porous membrane electrolyte enabled by poly(biphenyl piperidinium triphenylmethane) for dendrite-free zinc anode with enhanced cycling life, *Chem. Eng. J.*, 2022, **437**, 135409.

20. X. Yang, W. Wu, Y. Liu, Z. Lin and X. Sun, Chitosan modified filter paper separators with specific ion adsorption to inhibit side reactions and induce uniform Zn deposition for aqueous Zn batteries, *Chem. Eng. J.*, 2022, **450**, 137902.

21. J. Niu, J. Cao, X. Zhang, D. Zhang, C. Yang, K. Lolupiman, Z. Zeng, X. Zhang and J. Qin, Titanium Nitride-Cellulose Nanofiber Composite Separator for Zn Anode Stability in Aqueous Batteries, *ACS Appl. Energy Mater.*, 2024, **7**, 7496-7504.

22. C. Yang, P. Woottapanit, Y. Yue, S. Geng, J. Cao, X. Zhang, G. He and J. Qin, Industrial Waste Derived Separators for Zn-Ion Batteries Achieve Homogeneous Zn(002) Deposition Through Low Chemical Affinity Effects, *Small*, 2024, **20**, 2311203.

23. Y. Liu, S. Liu, X. Xie, Z. Li, P. Wang, B. Lu, S. Liang, Y. Tang and J. Zhou, A functionalized separator enables dendrite-free Zn anode via metal-polydopamine coordination chemistry, *InfoMat*, 2023, **5**, e12374.

24. J. Ma, X. Shi, Z. Wang, L. Zhou, X. Liu, X. Lu and Z. Jiang, High-Capacity Zinc Anode Enabled by a Recyclable Biomass Bamboo Membrane Separator, *Adv. Mater.*, 2024, **36**, 2406429.

25. Y. Dong, W. Liu, C. Carlos, Z. Zhang, J. Li, F. Pan, J. Sui and X. Wang, Active Dendrite Suppression by Ferroelectric Membrane Separators in Rechargeable Batteries, *Nano Lett.*, 2024, **24**, 4785-4792.

26. Y. Lei, Q. Li, Q. Liu, Y. Zeng, J. Li, W. Huang, F. Wang, S. Zhong and D. Yan, Low-cost separator with dust-free fabric composite cellulose acetate toward stable dendrite-free aqueous zinc-ion batteries, *Chem. Eng. J.*, 2024, **479**, 147846.

27. Z. Li, X. Wu, X. Yu, S. Zhou, Y. Qiao, H. Zhou and S.-G. Sun, Long-Life Aqueous Zn–I_2 Battery Enabled by a Low-Cost Multifunctional Zeolite Membrane Separator, *Nano Lett.*, 2022, **22**, 2538-2546.

28. H. Yu, X. Cai, Z. Wang, Z. Yang, W. Liu, M. Ren, J. Yao, Q. Liu and C. Qiao, High-performance rechargeable aqueous zinc-iodine batteries via a dual strategy of microporous carbon nanotubes for cathodic iodine immobilization and modified separator, *Colloids Surf., A*, 2024, **684**, 133239.

29. J. Kumankuma-Sarpong, C. Chang, J. Hao, T. Li, X. Deng, C. Han and B. Li, Entanglement Added to Cross-Linked Chains Enables Tough Gelatin-Based Hydrogel for Zn Metal Batteries, *Adv. Mater.*, 2024, **36**, 2403214.

30. Y. Xiong, H. Cheng, Y. Jiang, Z. Fan, X. Li, G. Wang, T. Liu and X. Gu, A novel water-reducer-based hydrogel electrolyte for robust and flexible Zn-I_2 battery, *Energy Storage Mater.*, 2025, **74**, 103981.